Shape-changing bodies in fluid: Hovering, ratcheting, and bursting

Saverio E. Spagnolie and Michael J. Shelley
Applied Mathematics Laboratory, Courant Institute of Mathematical Sciences, New York University, New York, New York 10012, USA

(Received 27 May 2008; accepted 14 November 2008; published online 6 January 2009)

Motivated by recent experiments on the hovering of passive bodies, we demonstrate how a simple shape-changing body can hover or ascend in an oscillating background flow. We study this *ratcheting* effect through numerical simulations of the two-dimensional Navier–Stokes equations at intermediate Reynolds number. This effect could describe a viable means of locomotion or transport in such environments as a tidal pool with wave-driven sloshing. We also consider the velocity burst achieved by a body through a rapid increase in its aspect ratio, which may contribute to the escape dynamics of such organisms as jellyfish. © *2009 American Institute of Physics*.
[DOI: 10.1063/1.3054143]

I. INTRODUCTION

The dynamics of bodies immersed in fluids is a subject of great practical and biological interest, and many aspects of active and passive flight, such as the dynamics related to vortex shedding and elastic-body/fluid interactions, continue to attract the attention of scientists and engineers. A special case of locomotion is hovering, in which a body subject to gravitational forces maintains its altitude with little average vertical displacement. The most common forms of hovering observed in nature, as employed by various birds and insects, involve the active passage of wings through the surrounding fluid at time-varying angles of attack in order to generate lift. It has been shown that quasi-steady fluid models do not entirely describe the fluid-body interactions in the hovering of various insects, such as locusts, sphingid moths, and dragonflies.[1–3] For a comprehensive review of the literature, see Wang.[4]

A related problem is assisted levitation, in which the settling of particles of fixed shape and size is arrested by the application of an oscillating background flow. Houghton[5] showed that it is theoretically possible in this setting to arrest a particle's downward sedimentation by considering a nonlinear drag law for the body motion. In related experimental work, the retardation of settling spheres in an oscillating column of water were studied by Baird *et al.*[6] and Tunstall and Houghton.[7] Variations on the type of background flow have also been explored. For example, Van Oeveren and Houghton[8] showed that particles may be driven upward against gravity by "sawtooth" oscillations where upward and downward flow accelerations differ, a result which was then shown numerically by Boyadzhiev.[9]

A less studied class of problems involves the dynamics of actively shape-changing bodies in fluids. Saffman[10] studied theoretically the self-propulsion of a deforming body in a perfect fluid. In order to study vortex shedding and other properties of hovering flight, Childress *et al.*[11] constructed and studied the hovering of passive, flexible "bugs" in an oscillating air column. A figure from that work is shown in Fig. 1, where smoke visualization was used to study the flow. The bottom illustration indicates the eddies observed in the experiments in relation to the body motion. As the body begins to move upward with the background flow, the "wings" passively extend, and the body shows a larger surface area to the upward moving flow. When the flow direction reverses, the wings close back toward the body, reducing the presented surface area, and shedding vortex pairs at the wing tips in the process. In order to focus solely on the vertical body displacements, the body is constrained to move vertically on a thin wire, although in Ref. 11, untethered, "free" hovering was also studied.

Motivated by this previous work, we consider shape-changing bodies moving in a viscous fluid. We discuss two instances of fluid/body interactions resulting from volume-preserving, shape-changing motions. First, we consider a ratcheting motion that may be experienced by an actively shape-changing body in a two-dimensional (2D) oscillating fluid. As in the experiments of Ref. 11 we find that the body can hover or even ascend against gravity. This effect could also describe a viable means of horizontal locomotion or transport in such environments as a tidal pool with wave-driven sloshing. We study the consequences of different temporal phase relations between the oscillating body and the background fluid motions. The body's velocity dynamics may be understood in the framework of basic drag-reduction/increase, although the resultant vortex generation and momentum transfer can be rather complex. Finally, we consider the velocity burst achieved by a body through a rapid increase in its aspect ratio, which may contribute to the locomotive dynamics of such organisms as jellyfish. This phenomenon is explored numerically for a variety of Reynolds numbers and body/fluid density ratios, and a momentum conservation argument is applied based on quasi-steady, virtual mass considerations, from which we recover the scalings observed in simulation.

II. EQUATIONS OF MOTION AND COMPUTATIONAL METHOD

We consider bodies with time-varying elliptical cross section (see Fig. 2) and compute their dynamics in a 2D Newtonian fluid. As suggested in Fig. 2 we consider only bodies moving up or down, with left-right and up-down symmetric deformations, and correspondingly left-right symmet-

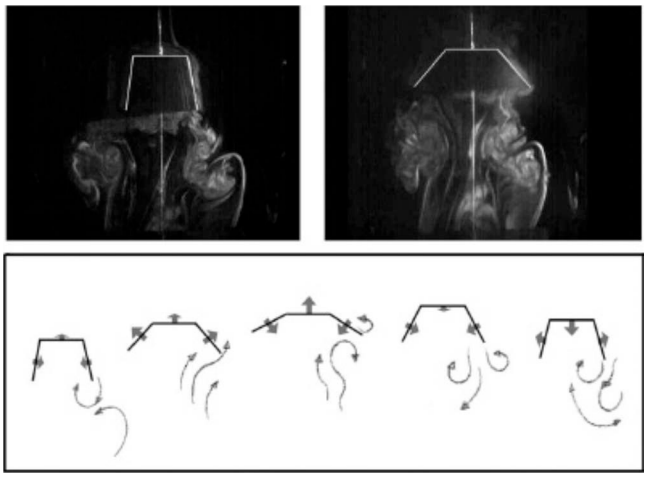

FIG. 1. Smoke visualization and illustration of a passive hovering "bug" from Childress *et al.* (Ref. 11); image reproduced with permission from Ref. 11, p, 4.

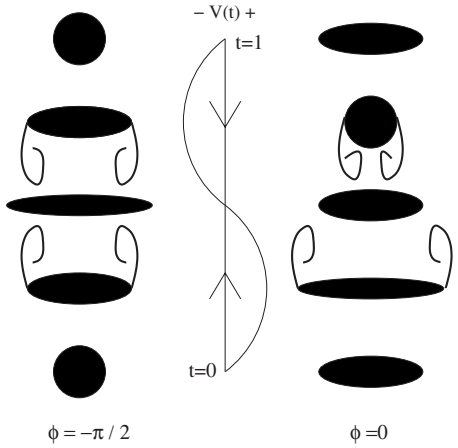

FIG. 2. Shape changing with phase difference (a) $\phi=-\pi/2$ and (b) $\phi=0$, relative to the background fluid velocity. The background flow velocity is $V(t)$, and we illustrate the drag asymmetry of interest. Case (b) can result in a sizeable net upward velocity.

ric fluid flows. We define the fluid velocity in the body frame, $\mathbf{u}^*$, relative to the body center of mass $\mathbf{x_0}(t)=y_0(t)\hat{\mathbf{y}}$, as $\mathbf{u}^*=\mathbf{u}-\dot{y}_0\hat{\mathbf{y}}$, where $\mathbf{u}$ is the fluid velocity in the laboratory frame and $\dot{y}_0$ is the vertical centroid velocity. The fluid mass and momentum conservation equations are given in the vorticity/stream formulation in the body frame as

$$\omega_t+\mathbf{u}^*\cdot\nabla\omega=\frac{\mu}{\rho}\Delta\omega \quad \text{in } \Omega, \tag{1}$$

$$\Delta\psi=\omega \quad \text{in } \Omega, \tag{2}$$

where $\omega=v_x-u_y$ is the vorticity, ψ is the stream function for the body-frame velocity $\mathbf{u}^*=\nabla^\perp\psi=(-\psi_y,\psi_x)$, μ is the viscosity, and ρ is the fluid density. Ω is the fluid domain, and we denote the body surface and fluid boundary by $\partial\Omega$. We assume that the background velocity in the laboratory frame has the form $V(t)\hat{\mathbf{y}}$ and that the vorticity is rapidly decaying. Hence, in the body frame we have

$$\omega(|\mathbf{x}|\to\infty,t)=0 \quad \text{and} \quad \nabla^\perp\psi(|\mathbf{x}|\to\infty,t)=[V(t)-\dot{y}_0]\hat{\mathbf{y}}. \tag{3}$$

Relative to the center of mass, we prescribe the body shape as $\mathbf{X}(\eta,t)=[x(\eta,t),y(\eta,t)]$, where $0\le\eta<2\pi$. The deformations will be area preserving and will generate a surface velocity $\mathbf{U}(\eta,t)$ in the body frame. Requiring the fluid velocity and surface velocity to match gives

$$\nabla^\perp\psi[\mathbf{x}=\mathbf{X}(\eta,t),t]=\mathbf{U}(\eta,t) \quad \text{on } \partial\Omega. \tag{4}$$

The fluid force on the body is determined by integrating the vertical fluid stress along its surface to yield

$$m\ddot{y}_0=\hat{\mathbf{y}}\cdot\oint\mathbf{T}\hat{\mathbf{n}}ds-mg, \tag{5}$$

where $\mathbf{T}=-p\mathbf{I}+\mu(\nabla\mathbf{u}+\nabla\mathbf{u}^T)$ is the fluid stress with p the fluid pressure, m is the body mass, g is the gravitational constant, and $\hat{\mathbf{n}}$ the outward-pointing unit normal vector on the body surface.

We assume a simple background flow, $V(t)=2\pi Af\sin(2\pi ft)$, having spatial amplitude A and temporal frequency f. We will also specify the body semimajor and semiminor axis lengths $L\cdot a(ft)$ and $L\cdot b(ft)$ and require that the body area $\text{Area}=\pi a(t)b(t)$ is constant, choosing $L=\sqrt{\text{Area}/\pi}$. [Hence, $a(t)b(t)=1$.]

We evolve these equations in a time-dependent, body-conforming coordinate system, a variation on an approach that has seen previous application.[12–14] Namely, we use elliptic-cylindrical coordinates (ξ',η) in a frame moving with the body,

$$x+iy=c(t)\cosh(\xi'+i\eta), \tag{6}$$

where $c(t)=\sqrt{a^2(t)-b^2(t)}$, $\xi'\in(0,\infty)$, and $\eta\in[0,2\pi)$. To fix a time-independent computational domain, the radial coordinate is rescaled as $\xi'=g(\xi,t)=\xi_0(t)+[\xi_B(t)-\xi_0(t)]\xi$. The time-dependent functions $\{\xi_0(t),\xi_B(t)\}$ are defined so that the coordinates $\xi=0$ and $\xi=1$ describe the time-varying body surface and outer computational boundary, respectively.

The system is nondimensionalized by scaling on the length L, velocity $U=Lf$, and time $T=L/U$. The system is then controlled by five dimensionless parameters/functions: the frequency Reynolds number $\text{Re}_f=\rho UL/\mu$, the Froude number $\text{Fr}=U/\sqrt{Lg}$, the amplitude ratio $A^*=A/L$, the mass ratio $M=m/\rho L^2$, and the time-dependent major axis length $a(t)$. An important remaining parameter is the phase difference ϕ, which relates the time course of the background flow oscillations to the deformation oscillations.

The nondimensionalized equations in the new coordinate system are

$$\omega_t-\dot{\mathbf{x}}|_\xi\cdot\nabla\omega+\frac{1}{J}\nabla^\perp\psi\cdot\nabla\omega=\frac{1}{Jg_\xi\text{Re}_f}(\omega_{\xi\xi}+g_\xi^2\omega_{\eta\eta}), \tag{7}$$

$$\psi_{\xi\xi}+g_\xi^2\psi_{\eta\eta}=Jg_\xi\omega, \tag{8}$$

where the Jacobian $J(\xi,\eta,t)=x_\xi y_\eta-x_\eta y_\xi$ is a time-dependent local scaling factor and $g_\xi=\xi_B(t)-\xi_0(t)$, both entering with the rescaling of the radial coordinate. The relative motion of points fixed in the (ξ,η) frame to the inertial frame intro-

duces an advection term, $\dot{\mathbf{x}}|_{\xi}\cdot\nabla\omega$ (see Ref. 15). The boundary conditions become

$$\omega(\xi\to\infty,\eta,t)=0, \tag{9}$$

$$\psi_{\xi}(\xi\to\infty,\eta,t)\sim[2\pi A^{*}\sin(2\pi t)-\dot{y}_0]x_{\xi}|_{\xi\to\infty}, \tag{10}$$

$$\psi(0,\eta,t)=\tfrac{1}{2}\dot{a}b\sin(2\eta), \tag{11}$$

$$\psi_{\xi}(0,\eta,t)=\tfrac{1}{2}(b\dot{b}-a\dot{a})\sin(2\eta). \tag{12}$$

A free integration constant in the description of ψ may be set to zero by a simple redefinition, since the stream function only enters the dynamics by its derivatives.

A convenient representation of the body acceleration is achieved by a manipulation of the velocity/pressure form of the Navier–Stokes equations. The translational body acceleration is rewritten in terms of the viscous drag $\mathbf{F}_{\nu}(t)$ and the pressure drag $\mathbf{F}_{\mathbf{p}}(t)$ as

$$M\ddot{\mathbf{x}}_0=\mathbf{F}_{\nu}(t)+\mathbf{F}_{\mathbf{p}}(t)-(M-\pi)\mathrm{Fr}^{-2}\hat{\mathbf{y}}, \tag{13}$$

where the viscous and pressure drag forces may be written as integrations against the vorticity and its normal derivative on the body surface, respectively (see Ref. 16),

$$\mathbf{F}_{\nu}(t)=\frac{1}{\mathrm{Re}_f}\int_0^{2\pi}\mathbf{x}_{\eta}\omega|_{\xi=0}d\eta, \tag{14}$$

$$\mathbf{F}_{\mathbf{p}}(t)=\pi\ddot{\mathbf{x}}_0-\frac{1}{\mathrm{Re}_f}\int_0^{2\pi}\mathbf{x}^{\perp}\left.\frac{\omega_{\xi}}{g_{\xi}}\right|_{\xi=0}d\eta. \tag{15}$$

The pressure drag includes an acceleration term due to the accelerating body frame. In an inviscid theory, the remaining component of the fluid pressure (here represented by the vorticity flux) also contributes a term proportional to $\ddot{\mathbf{x}}_0$, and the like terms combine to give an added mass. Formally, both types of drag are generated by the viscosity, but the distinction is useful because they are each generated by different flow phenomena. The viscous drag is generated by the no-slip condition on the body and corresponds to the development of a boundary layer near the surface. The pressure drag is associated with the wake that forms behind a bluff body and is generally less sensitive to the Reynolds number than the viscous drag. For flow past a circular cylinder at Reynolds number 100, experiments and simulations have shown that approximately 80% of the total drag is due to the pressure drag.[17,18]

Equation (13) verifies that gravity drops out of the dynamics when the body is density matched to the fluid, $M=\pi$. In the event that $M=\pi$, this equation reduces to a condition on the vorticity and its flux through the boundary. We choose $M>\pi$ to retain Eq. (13) as a prognostic equation for the body acceleration.

A. Numerical method

A mixed Fourier/finite-difference discretization is applied to the fluid equations. The computational grid is generated by uniform discretizations with $N_1\times N_2$ points by $(\xi_i,\eta_j)=(i\Delta\xi,j\Delta\eta)$, $(\Delta\xi,\Delta\eta)=[1/(N_1-1),2\pi/N_2]$. Derivatives in ξ are computed using fourth-order difference formulas; derivatives in η are computed with spectral accuracy in Fourier space. A second-order implicit Crank–Nicholson scheme is used for time stepping on the linear terms, and second-order Adams–Bashforth on the advection term. A uniform discretization in ξ places an increased density of physical mesh points near the body surface in this coordinate system, where the vorticity and its derivatives are most important to the dynamics. Fixing the number of grid points, further resolution of near-body dynamics may be achieved (at the expense of far-field resolution) by making a different choice for $g(\xi,t)$, although a nonlinear scaling here will add extra terms to the fluid equations.

The boundary conditions are treated implicitly, so that the boundary values of ω on the surface and ψ in the far field are part of the linear system to be solved; explicit treatment of the boundary conditions leads to a constrictive Courant–Friedrichs–Lewy condition for stability.[12] The vorticity is set to zero on the outer boundary at $\xi=1$, which is chosen at a distance from the body to ensure that the vorticity does not approach the boundary for the duration of computation. Finally, the two stated boundary conditions for ψ on the body surface are used to generate a numerical boundary condition for the vorticity there. Defining the shorthand $\psi_{i,j}=\psi(i\Delta\xi,j\Delta\eta)$, the discretized Poisson equation (8) relating ω and ψ on the boundary yields

$$\omega_{0,j}=\frac{g_{\xi}(0)}{J_{0,j}}(\psi_{\eta\eta})_{0,j}+\frac{1}{g_{\xi}(0)J_{0,j}\Delta\xi^2}\left[-\frac{85}{18}\psi_{0,j}+6\psi_{1,j}-\frac{3}{2}\psi_{2,j}+\frac{2}{9}\psi_{3,j}-44\Delta\xi(\psi_{\xi})_{0,j}\right]. \tag{16}$$

This expression results from the combination of two separate fourth-order discretizations of the no-slip condition on the body surface,

$$(\psi_{\xi})_{0,j}=\frac{1}{12\Delta\xi}(\psi_{-2,j}-8\psi_{-1,j}+8\psi_{1,j}-\psi_{2,j}), \tag{17}$$

$$(\psi_{\xi})_{0,j}=\frac{1}{12\Delta\xi}(-3\psi_{-1,j}-10\psi_{0,j}+18\psi_{1,j}-6\psi_{2,j}+\psi_{3,j}), \tag{18}$$

and the fourth-order discretization of the second derivative in ξ,

$$(\psi_{\xi\xi})_{0,j}=\frac{1}{12(\Delta\xi)^2}(-\psi_{-2,j}+16\psi_{-1,j}-30\psi_{0,j}+16\psi_{1,j}-\psi_{2,j}). \tag{19}$$

The "ghost points" $\psi_{-2,j}$ and $\psi_{-1,j}$ are determined by the single derivative expressions. Derivatives in the radial ξ direction are computed in the fluid bulk using the discretizations of Eqs. (18) and (19). Since ψ, ψ_{ξ}, and $\psi_{\eta\eta}$ are known on the body surface, the vorticity boundary condition is set by ψ values internal to the fluid. For bodies of fixed shape ($\dot{a}=\dot{b}=0$), Eq. (16) reduces to Briley's method.[19,20]

A generalized minimum residual (GMRES) iterative scheme[21] was constructed to solve the large linear system to

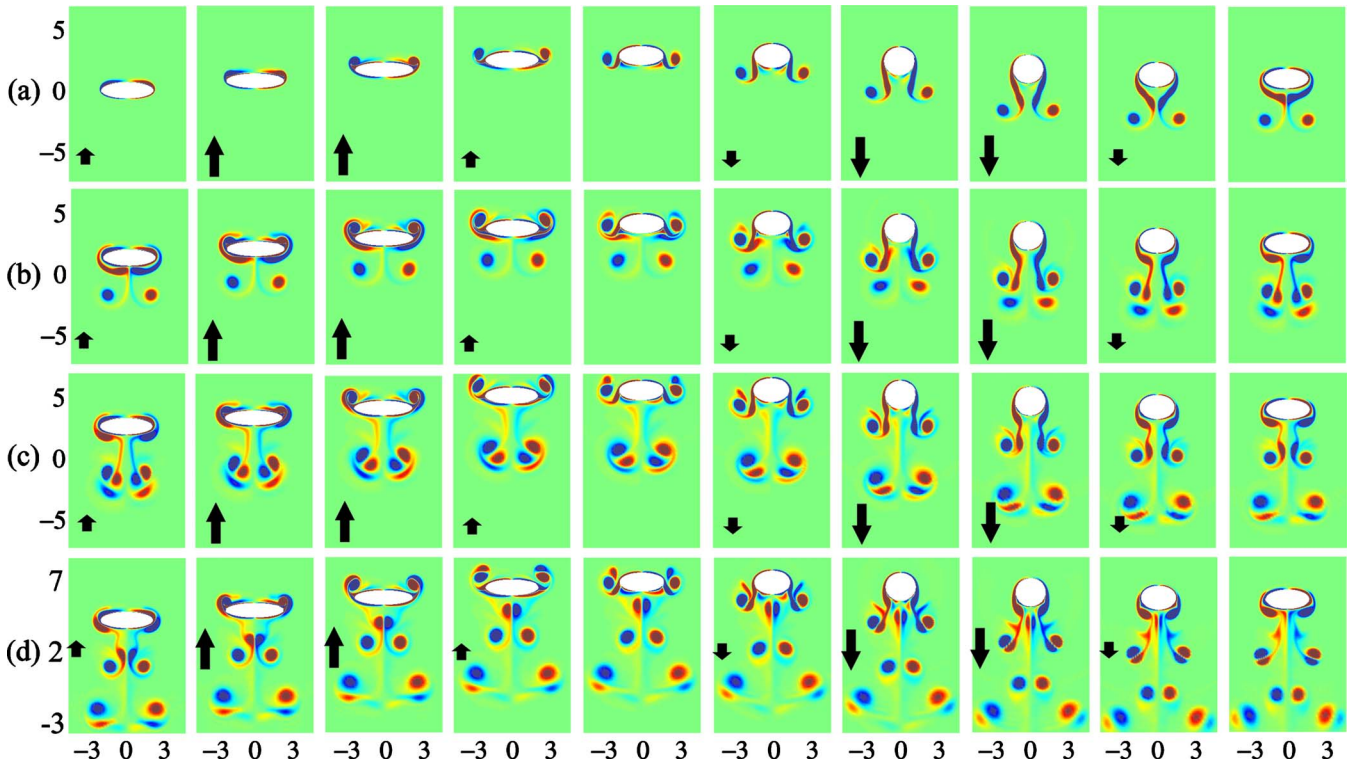

FIG. 3. (Color online) The vorticity generated over the first four oscillation periods, for $\mathrm{Re}_f=40$, $M=4\pi$, $\mathrm{Fr}=1$, $A^*=2$, and $\phi=0$. The images are equally spaced in time by a spacing $\Delta t=0.1$: $t\in[0.1,1]$ (a); $t\in[1.1,2]$ (b); $t\in[2.1,3]$ (c); and $t\in[3.1,4]$ (d). Note the vertical axis shift in row (d). The arrows indicate the direction of the background flow. The net-upward velocity due to shape changing dominates the gravitational effects.

a small error tolerance (10^{-7}). Further decreasing this tolerance did not alter the simulation results, so the numerical errors are due to discretization only. While Gaussian elimination requires $O(N^3)$ flops to invert an $N\times N$ matrix, GMRES requires only $O(N^2m)$, where m is the number of iterative steps, a large savings for large, well-conditioned matrices. The iterations converge to within the specified tolerance in approximately 20–200 iterations. Effective preconditioning is achieved by inverting a nearby linear system $Mx=b$ that is less expensive to invert than the original system, but retains the stiffest components. Preconditioning is achieved by solving the following fluid equations at each time step $t=t_n$, given a known right-hand side **b** (see Ref. 22),

$$\omega_t-\frac{1}{\mathrm{Re}_f}\Delta\omega=b_1(\xi,\eta)\quad\text{in }\Omega,\tag{20}$$

$$\Delta\psi-\omega=b_2(\xi,\eta)\quad\text{in }\Omega.\tag{21}$$

The boundary conditions used in the preconditioning problem are

$$\psi(0,\eta,t_n)=b_3,\quad \psi(1,\eta,t_n)=b_4,\tag{22}$$

$$\omega(0,\eta,t_n)=b_5,\quad \omega(1,\eta,t_n)=b_6.\tag{23}$$

The body acceleration in the preconditioning problem is simply $\dot{y}_0(t_n)=b_7$. The inner boundary condition (from Briley's method) is not used in the preconditioner, and the nonlinear advective term is also removed. Hence, the preconditioning problem decouples the equations for ω and ψ.

III. A FLUID RATCHET

We begin our investigation of a shape-changing body interacting with a fluid by examining a particular means of hovering or locomotion in an oscillating fluid. We set $a(t)=\left[\frac{3}{2}+\frac{1}{2}\sin(2\pi t+\phi)\right]+0.01$, with $b(t)=1/a(t)$; note that both the shape-changing and the background oscillations have the same temporal frequency, and that ϕ is a phase difference between them. Choosing $a(t)>b(t)$ avoids a singularity in the coordinate-system mapping. As illustrated in Fig. 2, the cross-sectional shape ranges from nearly circular to oblate with aspect ratio of approximately 4:1. Given these forms of $V(t)$ and $a(t)$, Fig. 2 also illustrates schematically

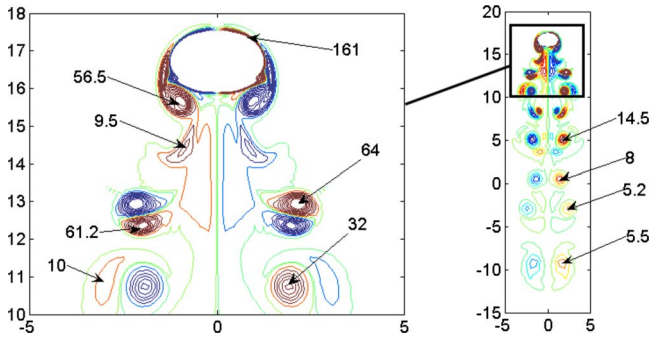

FIG. 4. (Color online) Vorticity contours after ten periods of oscillation, in a continuation of Fig. 3. The wake behind the ratcheting body is indicative of upward thrust, with vorticity pairs sending momentum downward into the fluid. Only positive vorticity is labeled, as the negative vorticity may be inferred by left-right symmetry.

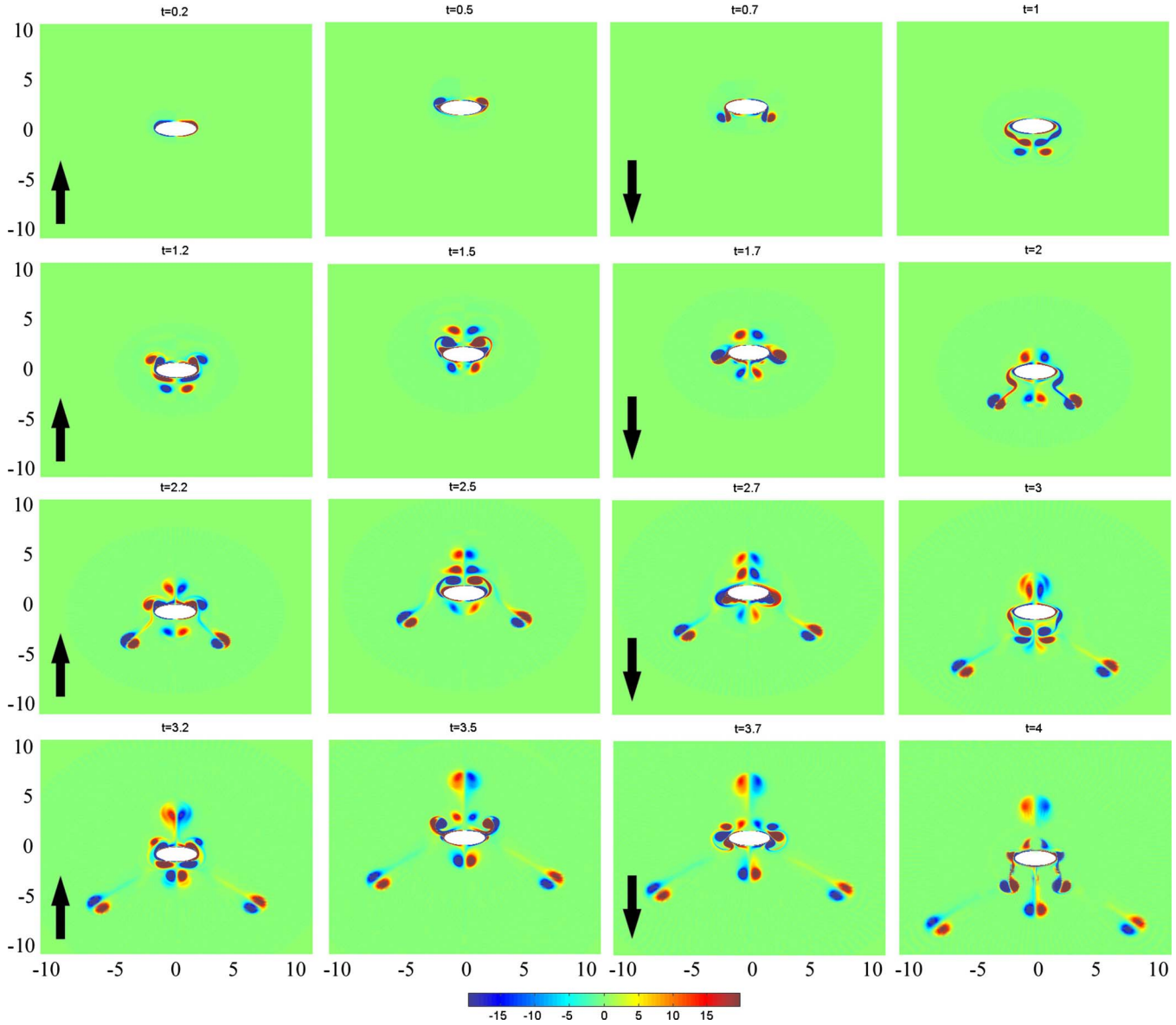

FIG. 5. (Color online) Early-stage vorticity production with $A=2$, $\mathrm{Fr}=1$, and $a(t)=1.5$ (no shape changing). The arrows indicate the velocity of the background flow.

the effect of ϕ. For $\phi=-\pi/2$, the body is the same oblate shape when the flow is at its strongest in either direction. We expect, and find, in this case that the body moves with zero or nearly zero net velocity. For $\phi=0$, $a(t)$ increases when the fluid flows upward $[V(t)>0]$, reaching its maximum as $V(t)$ realizes its own, and decreases when the flow is in the direction of gravity, reaching its most compact form as $V(t)$ becomes most negative. This is similar to the shape/flow relationship observed in the hovering experiments of Childress *et al.*[11]

This basic relation can cause the body to ratchet upward over each cycle, as demonstrated in Fig. 3; here, $\mathrm{Re}_f=40$, $M=4\pi$, $A^*=2$, $\phi=0$, and $\mathrm{Fr}^{-1}=1$ so that the body experiences a downward gravitational force. Initially the fluid is quiescent, $\omega(\mathbf{x},t=0)=0$, and the body is centered at the origin with zero velocity, $y_0(0)=\dot{y}_0(0)=0$. The generation of vorticity over these first four oscillation periods is remarkable both for its beauty and its complexity. For $t\in(0,0.5)$ [the first four panels of strip (a)] the flow is moving upward and acts to drive the body in the same direction, although with a smaller velocity due to the body inertia. The velocity difference between the flow and the body introduces a local shear at the body surface due to the no-slip condition, and the resultant vorticity is partially advected into the bulk fluid. Note that the ratio $A^*=A/L$ of fluid displacement to the characteristic body length is here only 2. Hence, the vortices do not separate an appreciable distance into the fluid on the updraft. The shed vorticity is positive on the right (counterclockwise rotations, in red online) and negative on the left (clockwise rotations, in blue online); this arrangement of the vorticity pair is characteristic of the wake behind a stationary body in a uniform stream.[23]

At $t=0.5$, the direction of the background flow is reversing, and the body is in the process of actively reducing its presented surface area. As the flow strengthens downward in the interval $[t\in(0.5,0.75)]$, the simultaneous reduction in

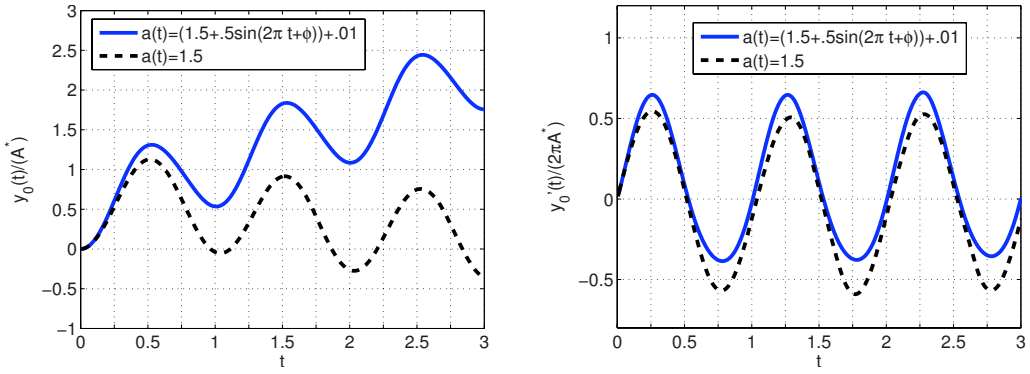

FIG. 6. (Color online) Left: The vertical positions of the shape changing and fixed aspect-ratio bodies are shown over the first three periods of background fluid oscillation. Right: The vertical velocities of both bodies during the same times.

body width separates the body from these vortices and also clears a path for them to be advected directly downward to well below the body. Meanwhile, two new "drag-type" vortices are created just below the body (again corresponding to those developed in the wake of a stationary body), but oppositely signed from the initial pair due to the opposite flow direction. The two sets of vortices also interact, and the newest vortex pair is entrained downward away from the body surface.

For $t \in (1,1.5)$ the flow is again moving upward. However, the body is presenting a greater profile to the fluid, and the most recently shed vortex pairs from below the body are not advected vertically without obstacle as before. Instead, they interact strongly with the body by rolling up around the sides and becoming intertwined with the new set of drag-type vortices being generated on the top surface (most visible at $t=1.5$). Then for $t \in (1.5,2)$, the fluid flows in the direction of gravity again, and the entire vorticity structure from above advects downward, once again with reduced obstruction.

In the following oscillation periods the same general trends repeat, although the interaction between the sequentially shed vortex pairs becomes more complex [note that the vertical axis is shifted upward in row (d)]. The primary vortical structure generated by these dynamics is downward moving vortex dipoles below the body, with positive vorticity (red online) on the right and negative vorticity (blue online) on the left. Unlike the oppositely signed drag-type vortex pairs, these dipoles are organized so as to correspond to a downward jet of fluid, which in turn allows the body to ascend vertically. We note that the positive vorticity on the right and negative vorticity on the left that pass down into the fluid are initially created as drag-type vortices when the flow is moving upward. The relationships between the upward moving flow, drag-type vorticity generation, and its subsequent passage down into the fluid for momentum transfer makes for an intricate and beautiful display.

The variable drag on the shape-changing body counteracts the effects of gravity in this regime, and the body has a net displacement upward over one period of flow oscillation. We refer to this fluid/body interaction as "ratcheting," since the body position oscillates with the fluid, but has a positive mean velocity in one direction and so increases its altitude with every period. Longer time dynamics are seen in Fig. 4, which shows the continuation of the simulation after ten oscillation periods. The vorticity dipoles induce downward velocities away from the body while spreading in time due to viscosity, leaving a wake indicative of upward thrust, with vortex dipoles periodically shuttling momentum downward into the fluid.

For comparison, we performed a similar simulation using a body of fixed shape, with $a(t)=1.5$, and using the same dimensionless parameters. The early-stage vorticity production for this body with fixed shape is shown in Fig. 5. Drag-type vortices are again formed above the body for $t \in (0,0.5)$. At $t=0.7$, the fluid is moving downwards and those vortices are passed down around the body as before, but not without obstacle: there is now a much stronger interaction between the body and the vortices than in the shape-changing body simulation. In a significant departure from the vorticity dynamics around the shape-changing body, the upward moving flow for $t \in (1,1.5)$ results in a vortical structure just above the surface at $t=1.5$ that is very similar to that below the body at $t=1$. An interesting feature of the vorticity production in this early stage is that two vortex dipoles are ejected to the bottom left and right, starting at approximately $t=2$. This is not seen in subsequent periods, so we attribute it to the specific form of the initial conditions. At longer times, dependence of the initial data diminishes, and there develops an approximate symmetry between the wakes above and be-

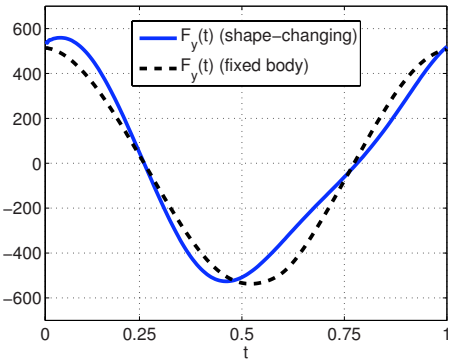

FIG. 7. (Color online) The total integrated vertical fluid stress $F_y(t)$ during the first oscillation on the shape changing and fixed bodies, as defined in the text.

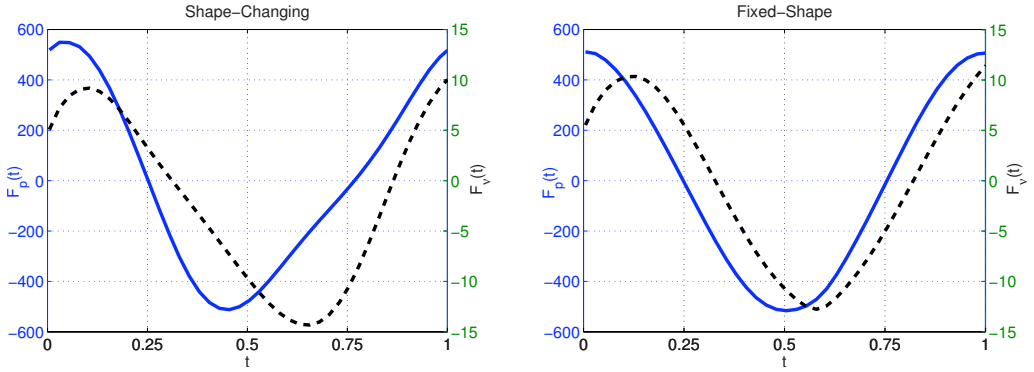

FIG. 8. (Color online) Left: The integrated pressure drag (left axis, solid line) and the much smaller viscous drag (right axis, dashed line) as functions of time for the shape-changing body. Right: The same, for the body of fixed shape.

low the body during upward and downward fluid flows, respectively. A new vortex quadrupole has developed just below the body at $t=3$, not unlike the new quadrupole seen just above the body at $t=2.5$. Similar vortex dipoles are seen to emanate further away from the body both upward and downward in $t \in [3.5,4]$, carrying momentum into the fluid, but in both directions. This lies in contrast to the strong up/down symmetry in Fig. 3, which leads to the development of only a downward moving fluid jet. The vertical positions and velocities from both the shape-changing and the fixed-body simulations are shown in Fig. 6. The fixed body descends on average, as there is no favorable asymmetry present for upward motility, unlike the ratcheting dynamics of the shape-changing body.

The total integrated vertical fluid stress $F_y(t)=\hat{\mathbf{y}}\cdot[\mathbf{F_p}(t)+\mathbf{F}_\nu(t)]$ during the first oscillation on each body example is presented in Fig. 7. For $t \in (0,0.25)$, the flow is accelerating upward, and the increased width of the shape-changing body leads to an increased net vertical fluid force. For $t \in (0.5,0.75)$, the flow is accelerating downward and the shape-changing body is more streamlined than the body of fixed shape; hence, the former experiences a smaller downward fluid force. Decomposing the vertical fluid force, we show the integrated pressure drag $F_p(t)=\hat{\mathbf{y}}\cdot\mathbf{F_p}(t)$ and viscous drag $F_\nu(t)=\hat{\mathbf{y}}\cdot\mathbf{F}_\nu(t)$ for both bodies in Fig. 8. The viscous drag on each body is smaller than the pressure or forms drag by an order of magnitude in this regime of motion.

The ratio A^* is a crucial parameter in determining whether the body rises or sinks against gravity. In Fig. 9 we show the results of a simulation identical to that in Fig. 3, except that the background flow amplitude is decreased by half to $A^*=1$. At first, the body sheds vortex pairs downward into the fluid as before and slowly begins to ascend. However, the gravitational acceleration eventually dominates these effects, and the body plummets (in mean) through its previously shed vortex pairs. Again, the vortical wake structure is striking.

If Fr^{-1} is decreased, or if A^* is increased, a shape-changing body can still maintain a positive upward mean velocity. This is shown in Fig. 10, where the normalized vertical positions are compared for simulations with $A^*=1$ and $A^*=2$ and with $\mathrm{Fr}=1$ and $M=\frac{3}{2}\pi$ for both. For $A^*=1$, as in the previously discussed simulation, the ratcheting mechanism is dominated by gravitational forces, and the body descends (in mean). The $\mathrm{Re}_f=20$ simulation involves larger fluid drag forces on the body in comparison to those at $\mathrm{Re}_f=80$, and the body descends faster in the higher Reynolds number simulation. For $A^*=2$, however, the ratcheting mechanism (by means of the increased fluid forces) dominates the gravitational effects, and the body maintains a positive mean velocity. Here we see that the $\mathrm{Re}_f=20$ and $\mathrm{Re}_f=80$ cases produce nearly identical results when normalized by the background oscillation amplitude, further underlining the subdominance of gravitational effects in this regime.

We now consider the ratcheting dynamics with zero gravitational force, $\mathrm{Fr}^{-1}=0$. In this case, for very low Reynolds numbers, $\mathrm{Re}_f \ll 1$, or separately for nearly density matched bodies, $M \approx \pi$, we observe little average vertical velocity. For any Re_f, nearly density matched bodies lead to very small mean velocities. If the body did not change shape, the body and fluid can move precisely together; in this event the fluid velocity has no spatial gradient, so the no-slip condition on the body does not alter the flow. The shape changing only plays a significant role in ratcheting when the body and fluid have different vertical velocities, so that viscous drag becomes relevant. The average and maximum vertical velocities obtained by ratcheting are shown in Figs. 11(a) and 11(b), normalized by the magnitude of background

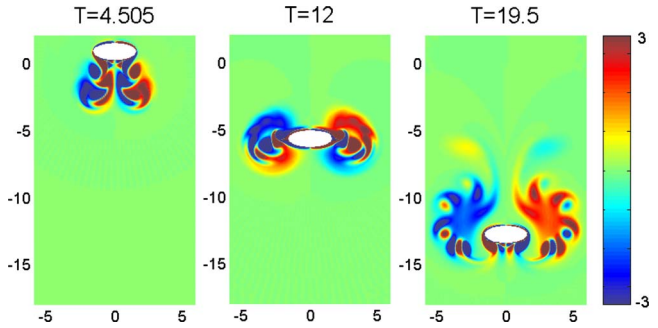

FIG. 9. (Color online) At $\mathrm{Re}_f=40$, $M=4\pi$, $A^*=1$, and $\mathrm{Fr}=1$, the ratcheting mechanism cannot overcome the effects of gravity, and the body descends (in mean), plummeting through the previously shed vortex pairs and creating this remarkable display.

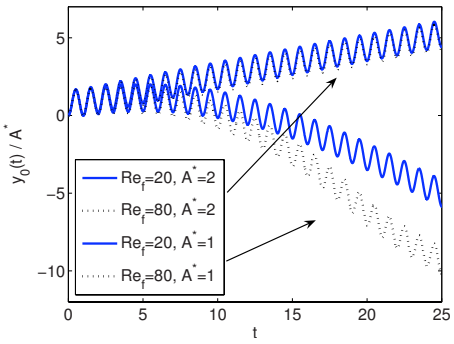

FIG. 10. (Color online) The body's normalized vertical position is shown for longer-time simulations with a gravitational field, Fr=1, and for two background oscillation amplitudes, $A^*=1,2$. Here $M=\frac{3}{2}\pi$.

fluid velocity. We vary M from $\pi+0.01$ to 4π and Re_f from 1 to 50.

Average and maximum velocities are computed only after the body oscillations are nearly periodic (the velocity returns after one period to within 0.1%). The results of these simulations are in agreement with the comments above. For low Reynolds numbers, and for nearly density matched bodies, the mean velocity tends toward zero, and the maximum velocity tends toward the bulk fluid velocity Af.

As the Reynolds number increases and the dynamics exit the Stokesian regime, fluid forces and vorticity begin to play more significant roles. Figure 11(a) indicates the existence of an optimal Reynolds number for ratcheting for a given body mass. For a fixed Reynolds number, Figs. 11(c) and 11(d) show that the average vertical velocity increases with body mass, while the maximum velocity decreases. Thus, a heavier body's larger inertia acts to smooth out the vertical motion, with the mean and maximum velocities appearing to converge to the same point. A simple analysis based on a square drag law suggests that $\langle \dot{y}_0(t) \rangle$ increases to a nonzero mean value with increasing mass, with a deviation decaying like $O(1/M^2)$. The analysis also suggests that the maximum mean velocity decays to the same mean velocity, deviating for large body mass like $O(1/M)$.

We expect some time lag in the momentum exchange, and to this end we explore the optimal phase difference between shape changing and fluid oscillation, the results of which are shown in Fig. 12. To develop these plots, we considered a range of phase differences ϕ for $\mathrm{Re}_f=40$ and masses $M=2\pi$ and $M=4\pi$. The simulations were allowed to run long enough for the body to settle into a periodic orbit, which generally occurred after only a few periods. In consideration of Fig. 2, one might suppose that the body has zero mean velocity for the relation $\phi=-\pi/2$. Instead, we observe a shift from this phase relationship: when the background oscillation and shape changing are exactly out of phase ($\phi=-\pi/2$) the mean velocity is actually positive. In this regime of Reynolds numbers and density ratios, we find that the extremal phases are $\phi\approx-0.35$ and $\phi\approx2.8$ (maximal net upward and downward velocities, respectively). We observe that increasing the body mass increases the mean vertical velocity, but does not significantly affect the phase relation. The maximum vertical velocity [Fig. 12(b)] decreases as expected for the more massive body. The minimum vertical velocity achieved is simply opposite the maximum, but shifted by $\phi\rightarrow\phi+\pi$.

For the simulations above, we have focused our attention

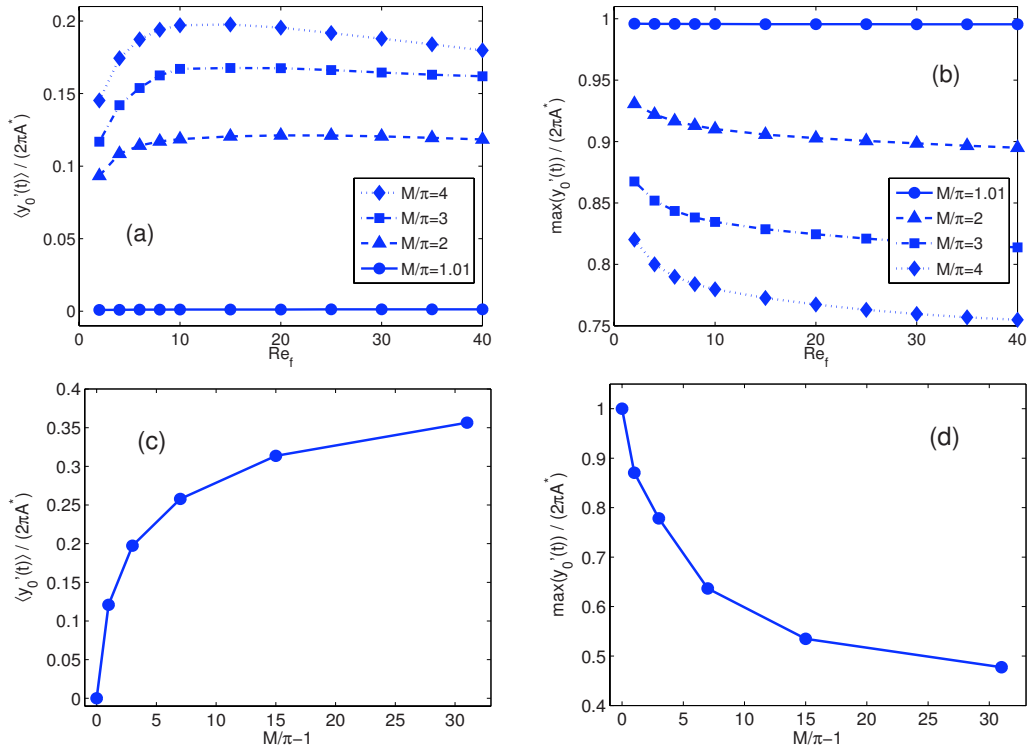

FIG. 11. (Color online) Mean (a) and maximum (b) vertical velocities are shown as functions of Reynolds number for four density ratios. We fix the phase $\phi=0$, the background flow $A^*=1$, and there is no gravity ($\mathrm{Fr}^{-1}=0$). Mean (c) and maximum (d) vertical velocities as functions of body mass for $\mathrm{Re}_f=10$.

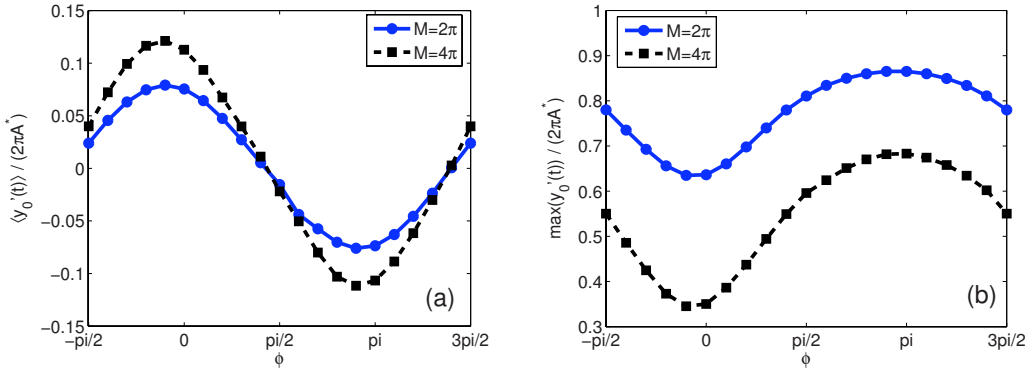

FIG. 12. (Color online) For two mass ratios, $M=2\pi$ and $M=4\pi$, the normalized mean (a) and maximal (b) velocities are shown as functions of the phase difference ϕ.

on the long-term dynamics and the periodic steady states into which the system settles after a number of oscillation periods. Different initial conditions for such systems, as performed in simulations not shown here, lead to different vorticity profiles and body dynamics during the first few periods of motion; however, the same periodic steady states are eventually achieved as the dependence of the initial data diminishes.

We note that in the Stokesian regime the ratcheting mechanism associated with an oscillating background flow disappears, but reappears upon the application of an oscillating external body force. For a constant body force such as gravity, exact solutions to the Stokes equations show that the body sediments at the same time-averaged rate as in the absence of an oscillating background flow.

IV. A VELOCITY BURST

Finally, we consider another aspect of this class of shape-changing dynamics, a velocity burst exhibited by a body elongating its shape. At intermediate to high Reynolds numbers, a body may temporarily but dramatically increase its speed in a mechanism that may be employed by some organisms taking evasive action.

We set $A^*=0$, $\mathrm{Fr}^{-1}=0$, and focus on horizontal motions in the direction of the elliptic major axis. The body is seeded with an "initial" horizontal velocity u_0 in a smooth ramp for $t\in[0,0.5)$, after which the motion is determined by its interaction with the fluid. The ramped velocity in this startup stage is $\dot{x}_0(t)=u_0\sin^2(\pi t)$. The body shape is prescribed as an elongation from one elliptic shape to another, with initial and final semimajor axis lengths a_0 and a_1,

$$a(t)=\begin{cases} a_0, & t<0.6,\\ \dfrac{a_1+a_0}{2}-\dfrac{a_1-a_0}{2}\cos[2\pi(t-0.6)], & t\in[0.6,1.1],\\ a_1, & t>1.1. \end{cases}$$

The corresponding initial and final semiminor axis lengths are $b_0=1/a_0$ and $b_1=1/a_1$, respectively. Hence, the body begins to elongate at $t=0.6$, shortly after the cessation at $t=0.5$ of the velocity ramp-up. We denote the body velocity at the conclusion of the elongation by $u_1=\dot{x}_0(t=1.1)$ and define a velocity burst as the ratio u_1/u_0. For these simulations, we replace Re_f by the Reynolds number $\mathrm{Re}=\rho a_0 u_0/\mu$, where velocity is scaled on u_0 and length on a_0.

We begin by considering a (nearly) density matched body, $M=1.01\pi$, which is seeded with an initial horizontal velocity $u_0=1$, and then expands from a circle of radius $a_0=1.01$ to an ellipse with $a_1=2.01$. For this simulation, $\mathrm{Re}=200$. The dimensionless body and horizontal fluid momenta ($\mathcal{M}_{\mathrm{body}}=M\hat{\mathbf{x}}_0$, $\mathcal{M}_{\mathrm{fluid}}=\hat{\mathbf{x}}\cdot\int_\Omega\nabla^\perp\psi dxdy$) are shown in Fig. 13, along with a schematic of the shape expansion. The body (directly) and the fluid (indirectly) are seeded with positive momenta during the ramp-up stage for $t\in[0,0.5)$. The body is then released, after which time the system's total momentum is conserved. The fluid drag is a force opposite the direction of body motion, and the momentum begins to transfer from the body to the fluid through the boundary layer at the surface. For $t\in(0.6,1.1)$, the body undergoes its shape-changing elongation, during which time the body recovers significant momentum from the fluid. The body velocity at the conclusion of this elongation (the velocity burst) is $u_1=1.34$. Finally, the body reaches its final shape and begins to decelerate again due to the fluid drag forces.

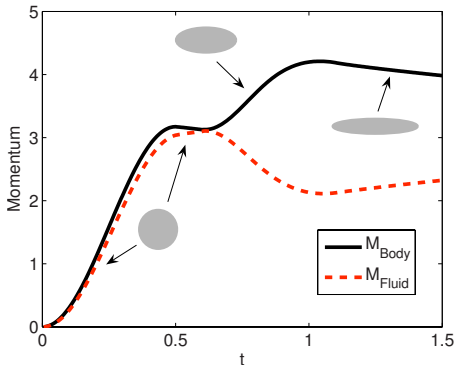

FIG. 13. (Color online) The body and fluid momenta for a velocity burst with $M=1.01\pi$ and $\mathrm{Re}_f=200$. A circle of radius $a_0=1.01$ and the surrounding fluid are seeded with positive momenta from $t=0$ to $t=0.5$ as the body is ramped up to an initial velocity $u_0=1$. At this time the body is released from external guidance, after which the total momentum is conserved as shown. The body begins to change shape at $t=0.6$ and has reached its final shape at $t=1.1$, during which the body experiences a burst in velocity to $u_1/u_0\approx1.34$. Finally, the body coasts and slows due to viscous drag.

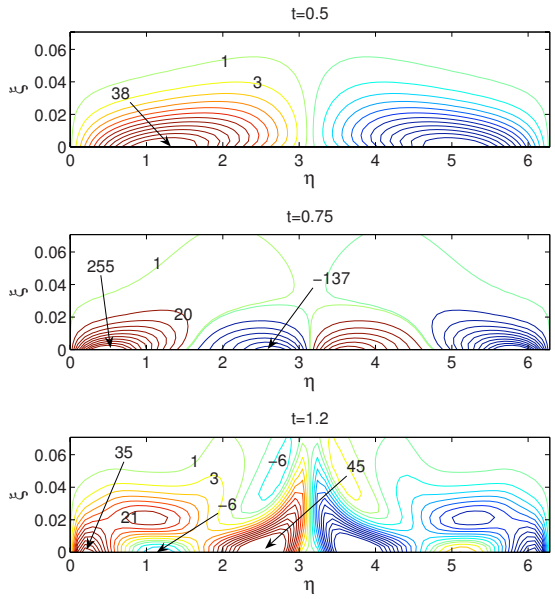

FIG. 14. (Color online) The vorticity before, during, and after body expansion for Re=200. $\xi=0$ gives the body surface. $\eta=0$ and $\eta=\pi$ correspond to the body's fore and aft, respectively.

The vorticity near the surface is shown before, during, and after the body expansion in Fig. 14. $\eta=0$ corresponds to the leading edge and $\eta=\pi$ corresponds to the aftmost point on the surface. At $t=0.5$ the circular body is released and enters a coasting stage, where it begins to decelerate. The smooth ramp-up to the initial velocity has generated a boundary layer of vorticity which is entirely connected to the surface. At $t=0.75$, the body is nearing its peak acceleration. The speed of the body's fore and aft surfaces relative to the center of mass is over three times larger than the initial coasting velocity as the body changes shape. The vortical structure is therefore determined primarily by the expansion (through the no-slip condition) and is seen here to correspond to four vortices of alternating sign around the body surface. At $t=1.2$ the body is in its final shape and is decelerating, although the unsteady expansion activity has left the vorticity dynamics in a transient state. Vortices have separated from the surface above and below the body during the expansion.

Figure 15 shows the horizontal fluid forces $\hat{\mathbf{x}}\cdot\mathbf{F}_{\mathbf{p}}(t)$ and $\hat{\mathbf{x}}\cdot\mathbf{F}_{\nu}(t)$. During the ramp-up stage, the external "push" generates a large negative force against the direction of motion. After the body has been released and begins to change shape, the positive net pressure force dominates the viscous force by two orders of magnitude. This force associated with the shape expansion gives a body acceleration or velocity boost to the right. This velocity boost effect likely contributes to the ratcheting mechanism, the subject of our previous inquiry. A clear comparison between the two is complicated by the background flow oscillation in that problem.

We will consider additional results of the simulations, but first we introduce a simplified model using potential theory and time-varying added-mass coefficients.

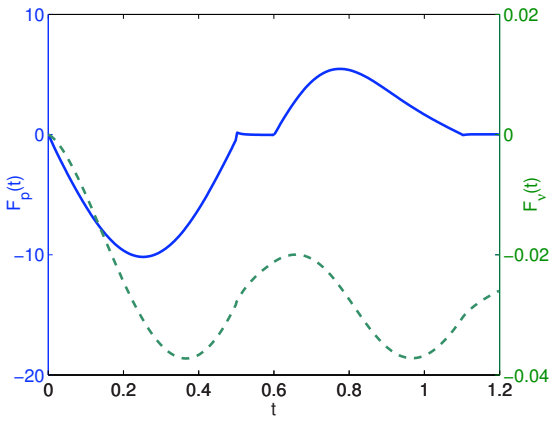

FIG. 15. (Color online) The integrated pressure force (left axis, solid line) and the much smaller viscous force (right axis, dashed line) as functions of time for $t\in(0,1.2)$.

A. Model: Potential flow and added mass

To develop a simplified model of the velocity burst effect, we assume a steady, irrotational, inviscid flow before and after expansion, so we have a potential function describing the fluid velocity everywhere. Applying potential theory, we are able to recover the trends found in simulations of this phenomenon using only conservation of momentum and using the appropriate added-mass coefficients.

An accelerating body is accompanied by a response in the surrounding fluid; a force accelerating the body must then also increase the fluid's kinetic energy. This effect is captured by a so-called acceleration reaction force that resists the motion (see Ref. 23). The acceleration reaction enters the dynamics in the form of an added mass, which any force on the body must accelerate in addition to the body mass. For a detailed discussion and computation of added masses for various simple shapes, see Ref. 24. The added mass for an ellipse moving in the direction of its major axis in a 2D fluid is equal to that of the inscribed circle, $\rho\pi b^2$.[24,25] We consider bodies with initial radius $a_0=1$ and final axis lengths a_1 and $b_1=1/a_1$ (area preserving). The initially seeded velocity and that just after expansion are u_0 and u_1, respectively. Here we assume that the expansion occurs quickly, and that the body moves with constant velocity in a steady potential flow just before and after expansion. The fluid momentum is then captured through the added mass, and a momentum conservation argument for the motion before and after expansion in this case gives

$$(M+\pi)u_0=(M+\pi b_1^2)u_1 \tag{24}$$

$$\Rightarrow\frac{u_1}{u_0}=\frac{M/\pi+1}{M/\pi+b_1^2}. \tag{25}$$

In this simplified model, we find that the velocity burst effect decreases with increasing body mass and increases with increasing final aspect ratio. In Fig. 16, we compare the results of this model with simulations at finite Reynolds numbers for a range of final expansion lengths. Here the body is (nearly) density matched, $M=1.01\pi$. We observe in the simulations a simple deviation of the velocity burst from

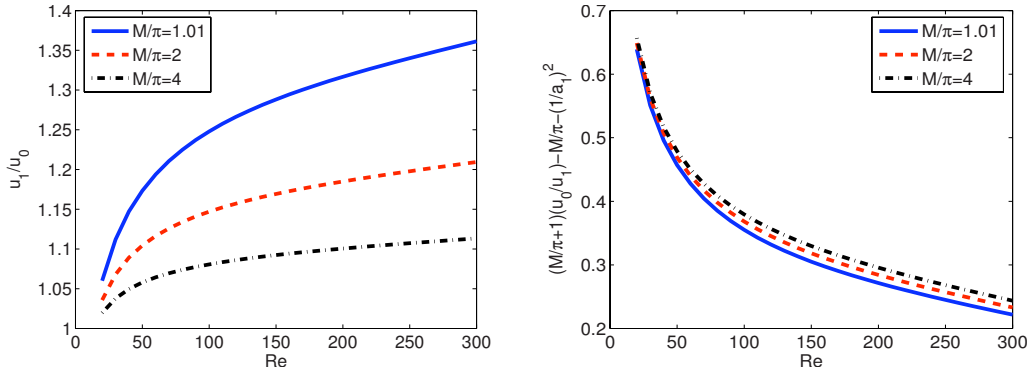

FIG. 16. (Color online) Left: Velocity burst magnitudes are shown in figure for a range of final semimajor axis lengths a_1, with $M=1.01\pi$. We include the velocity burst predicted by potential theory (with $a_0=1$). Right: We isolate the deviation from the potential theory with the scaling implied by the analytic result.

that predicted by the added-mass model for intermediate to high Reynolds numbers. The deviation is a function of density ratio and Reynolds number which we denote by $c(\mathrm{Re},M)$,

$$\left(\frac{M}{\pi}+1\right)\left(\frac{u_0}{u_1}\right)-\frac{M}{\pi}\approx b_1^2+c(\mathrm{Re},M) \tag{26}$$

$$\Rightarrow \frac{u_1}{u_0}=\frac{M/\pi+1}{M/\pi+b_1^2+c(\mathrm{Re},M)}. \tag{27}$$

The velocity burst is plotted as a function of Reynolds number for a few density ratios in Fig. 17. In the left plot we note that the deviation does not appear to vary significantly with the density ratio, thus $c(\mathrm{Re},M)\approx c(\mathrm{Re})$; also, we find that $c(\mathrm{Re})$ is a decreasing function, possibly limiting to zero (as potential theory suggests). For this range of density ratios and Reynolds numbers, we find approximately $c(\mathrm{Re})\approx 1.8\ \mathrm{Re}^{-0.34}$.

Finally, given the same assumptions, we give the results for a sphere expanding into a prolate ellipsoid in the direction of motion in three dimensions. We redefine the dimensionless length $L=\left[\mathrm{Volume}/\left(\frac{4}{3}\pi\right)\right]^{1/3}$, and mass ratio $M=m/(\rho L^3)$. (The body is density matched to the fluid for $M=4\pi/3$.) We consider a sphere of radius $a_0=1$, shape changing into an ellipsoid with one axis length a_1, and the other minor-axis lengths each $b_1=\sqrt{a_0^3/a_1}$ (volume preserving). $(a_1>b_1)$ is a prolate ellipsoid, while $(a_1<b_1)$ is an oblate ellipsoid. The added mass for such a body moving in the direction of the a_1 axis may be written in the nondimensionalized system as $M_a=\frac{4}{3}\pi\kappa(a_1/b_1)$, where (see Ref. 25)

$$\kappa(r)=-\frac{Z(r)+1/r}{Z(r)+r},\quad Z(r)=\frac{\log(r-\sqrt{r^2-1})}{\sqrt{r^2-1}}. \tag{28}$$

The coefficient $\kappa(r)$ is shown in Fig. 18. For a sphere, $\kappa(1)=1/2$, and the added mass is half the displaced fluid mass, $M_a=2\pi/3$. The velocity burst (for sphere-to-prolate expansion) or deceleration (for sphere-to-oblate contraction) may then be written

$$\frac{u_1}{u_0}=\frac{3M+2\pi}{3M+4\pi\kappa(a_1/b_1)}. \tag{29}$$

Since $\kappa(r)\to\infty$ for $r\to 0$, we find that a shape-changing body may theoretically slow itself to an arbitrarily small velocity by fanning out to a large flat disk. For a sphere expanding into a prolate ellipsoid in the direction of the major axis, an upper bound on the velocity burst is

$$\lim_{b_1\to 0}\frac{u_1}{u_0}=1+\frac{2\pi}{3M}. \tag{30}$$

The acceleration reaction can dominate the forces resisting rapid body accelerations and has been the focus of a number

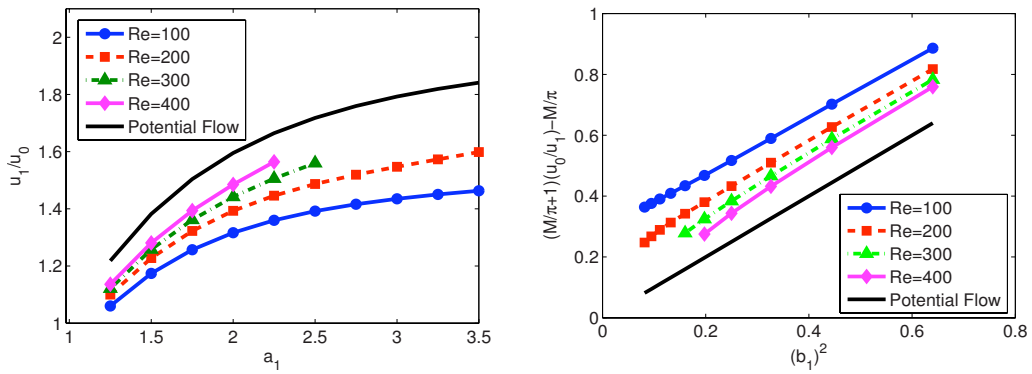

FIG. 17. (Color online) Left: The velocity burst is shown as a function of Reynolds number for three mass ratios M. Right: The deviation from the velocity burst predicted by the added-mass model, $c(\mathrm{Re},M)$.

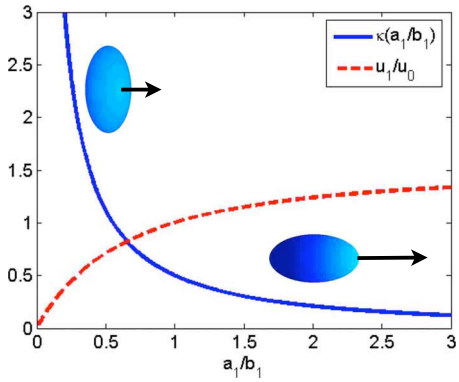

FIG. 18. (Color online) The added-mass coefficient $\kappa(r)$ for a sphere to a three-dimensional ellipsoid, as well as the velocity burst/brake with $M=4\pi/3$.

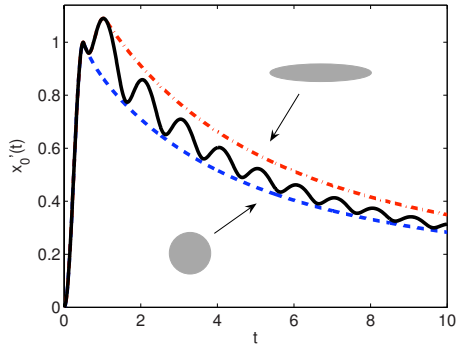

FIG. 19. (Color online) A body with a prescribed, periodic shape change at Re=40 does not exhibit locomotive behavior, as shown by a velocity comparison to coasting, decelerating bodies of constant aspect ratio. The bodies are initially ramped up to velocity $u_0=1$, and are then released. The periodic shape changing begins at $t=0.6$, but ceases for the ellipse of subsequently fixed shape at $t=1.1$.

of studies.[26–31] These works pay particular attention to jellyfish, aquatic invertebrates, which locomote by the unsteady ejections of fluid jets from their bells. The acceleration reaction is a shape-dependent force. Thus, many authors have noted that a reduced virtual mass corresponds with a reduced acceleration reaction and that an organism's escape acceleration is aided therefore by a slender profile. Daniel[26] and Donaldson and Mackie[32] showed that medusae utilizing escape responses are generally prolate with length/diameter ratios greater than 2, and consequently have added-mass coefficients less than 0.2. Here we have shown something different. While a reduced virtual mass gives a reduced acceleration reaction, a *reducing* virtual mass can generate a boost in velocity. The effects of a time-varying added mass have previously been accounted for in simplified models of jellyfish locomotion by Daniel[27] and Dabiri and Gharib.[31] We will be interested to learn how this velocity burst enters into the dynamics of such invertebrate organisms, as a component of the total acceleration, at finite Reynolds numbers.

V. CONCLUSION

We have shown that a shape-changing body can hover or ascend in a particular fluid regime by shuttling momentum-carrying vortex dipoles downward into the fluid. These vortex dipoles are created above the body during the updraft and are advected with reduced obstruction downward into the fluid when the body becomes more streamlined and the background flow reverses direction. We find that in the absence of gravity, mean velocities actually increase with the body mass, which stabilizes the motion, and allows for a larger drag discrepancy between the updraft and downward moving flows. Future work will explore the space (A^*,Fr) to determine the background flow requirements for hovering relative to the gravitational effects.

The class of problems categorized by shape-changing bodies in fluids is vast and complex, and there are still many avenues to explore in the problems discussed here alone. The ratcheting dynamics should extend naturally to three dimensions, although the study of such phenomena requires the application of alternative numerical methods. In this work we have considered only active shape changing, where the body shape is a prescribed. A simple extension of this work will consider passive shape-changing, in which the fluid forces determine to some extent the shape of the body. This will connect the simulations more closely to the experimental work of Childress *et al.*,[11] where the body shape is dictated by interactions with the fluid.

Another question of future interest regards the stability of shape-changing bodies in various flow fields. The interactions of bodies with previously shed wakes can generate rich and interesting dynamics, such as the symmetry breaking instability which leads to a sustained horizontal motion in flapping flight (see Alben and Shelley[14]). The stability of the ratcheting motion is unclear when the body is free to move horizontally, although the hovering experiments of Childress *et al.* were surprisingly robust.[11,33] This issue will be the subject of a subsequent paper.

The velocity burst dynamics discussed herein were happened upon while studying a separate problem, not discussed in detail here. In this related problem, a body with a prescribed, periodic shape change (from a circle to an ellipse and back, repeated) is set in an otherwise quiescent fluid. The body elongation produces two vortex pairs (as in Fig. 14), and it seemed feasible that this structure may lend itself to a symmetry breaking instability, leading to a sustained horizontal motion (again, see Ref. 14). Figure 19 shows the body's horizontal velocity for one such simulation. A circular body is ramped up to an initial velocity $u_0=1$ for $t\in(0,0.5)$ and begins to change shape at $t=0.6$. The velocity burst of our subsequent study may be seen shortly thereafter. For comparison, Fig. 19 includes the coasting velocities of the circle and ellipse at the extremes of the shape-changing motion. The long time dynamics indicate that the shape-changing body slows, in this case with a velocity bounded by those of the related fixed-shape bodies. At least over the class of aspect-ratio profiles considered, we do not observe the sustained locomotive dynamics of our initial inquiry. We explored a range of body masses and Reynolds numbers from Re=1 to Re=400, and the dynamics were qualitatively similar to those shown in Fig. 19. However, we do suspect that the same symmetric motions could lead to coherent horizontal locomotion if the body is instead placed in a shear thin-

ning fluid. When the body is moving through the fluid, the elongation from the circular to the elliptic shape in the direction of motion introduces an asymmetry in the speed of the fore and aft surfaces in the laboratory frame. The fluid stress on the body's (faster moving) leading edge may vary significantly from that at the (slower moving) aft, and the asymmetry might generate a sustained capacity for horizontal locomotion. Future studies will examine this and other applications of shape-changing bodies in non-Newtonian fluid environments.

ACKNOWLEDGMENTS

The authors thank Steve Childress and Jun Zhang for fruitful discussions. Funding from the Department of Energy (Grant No. DE-FG02-88ER25053) is also gratefully acknowledged.

[1] M. Cloupeau, J. F. Devillers, and D. Devezeaux, "Direct measurements of instantaneous lift in desert locust: comparison with Jensen's experiments on detached wings," J. Exp. Biol. **80**, 1 (1979).
[2] P. J. Wilkin and M. H. Williams, "Comparison of the instantaneous aerodynamic forces on a sphingid moth with those predicted by quasi-steady aerodynamic theory," Physiol. Zool. **66**, 1015 (1993).
[3] J. Z. Wang, "The role of drag in insect hovering," J. Exp. Biol. **207**, 4147 (2004).
[4] J. Z. Wang, "Dissecting insect flight," Annu. Rev. Fluid Mech. **37**, 183 (2005).
[5] G. Houghton, "The behaviour of particles in a sinusoidal velocity field," Proc. R. Soc. London, Ser. A **272**, 33 (1963).
[6] M. H. I. Baird, M. G. Senior, and R. J. Thompson, "Terminal velocities of spherical particles in a vertically oscillating liquid," Chem. Eng. Sci. **22**, 551 (1967).
[7] E. B. Tunstall and G. Houghton, "Retardation of falling spheres by hydrodynamic oscillations," Chem. Eng. Sci. **23**, 1067 (1968).
[8] R. M. Van Oeveren and G. Houghton, "Levitation and counter-gravity motion of spheres by non-uniform hydrodynamic oscillations," Chem. Eng. Sci. **26**, 1958 (1971).
[9] L. Boyadzhiev, "On the movement of a spherical particle in vertically oscillating liquid," J. Fluid Mech. **57**, 545 (1973).
[10] P. G. Saffman, "The self-propulsion of a deformable body in a perfect fluid," J. Fluid Mech. **28**, 385 (1967).
[11] S. Childress, N. Vandenberghe, and J. Zhang, "Hovering of a passive body in an oscillating airflow," Phys. Fluids **18**, 117103 (2006).
[12] W. E and J.-G. Liu, "Essentially compact schemes for unsteady viscous incompressible flows," J. Comp. Physiol. **126**, 122 (1996).
[13] U. Pesavento and J. Wang, "Falling paper: Navier–Stokes solutions, model of fluid forces, and center of mass elevation," Phys. Rev. Lett. **93**, 144501 (2004).
[14] S. Alben and M. Shelley, "Coherent locomotion as an attracting state for a free flapping body," Proc. Natl. Acad. Sci. U.S.A. **102**, 11163 (2005).
[15] J. F. Thompson, Z. U. A. Warsi, and C. W. Mastin, *Numerical Grid Generation* (Elsevier Science, New York, 1985).
[16] S. E. Spagnolie, "Flapping, ratcheting, bursting, and tumbling: A selection of problems in fluid-body interaction dynamics," Ph.D. thesis, New York University, 2008.
[17] A. Roshko, "Experiments on the flow past a circular cylinder at very high Reynolds number," J. Fluid Mech. **10**, 345 (1961).
[18] M. Braza, P. Chassaing, and H. Ha Minh, "Numerical study and physical analysis of the pressure and velocity fields in the near wake of a circular cylinder," J. Fluid Mech. **165**, 79 (1986).
[19] W. Briley, "Numerical study of laminar separation bubbles using Navier–Stokes equations," J. Fluid Mech. **47**, 713 (1971).
[20] W. E and J. Liu, "Vorticity boundary conditions and related issues for finite difference schemes," J. Comput. Phys. **124**, 368 (1996).
[21] Y. Saad and M. H. Schultz, "GMRES: a generalized minimal residual algorithm for solving nonsymmetric linear systems," SIAM (Soc. Ind. Appl. Math.) J. Sci. Stat. Comput. **7**, 859 (1986).
[22] R. Barrett, M. Berry, T. F. Chan, J. Demmel, J. Donato, J. Dongarra, V. Eijkhout, R. Pozo, C. Romine, and H. Van der Vorst, *Templates for the Solutions of Linear Systems: Building Blocks for Iterative Methods*, 2nd ed. (SIAM, Philadelphia, 1994).
[23] G. K. Batchelor, *An Introduction to Fluid Dynamics* (Cambridge University Press, Cambridge, 1967).
[24] C. Yih, *Fluid Mechanics* (McGraw-Hill, New York, 1969).
[25] N. E. Kochin, I. A. Kibel, and N. V. Rose, *Theoretical Hydromechanics* (Interscience, New York, 1964).
[26] T. L. Daniel, "Unsteady aspects of aquatic locomotion," Am. Zool. **24**, 121 (1984).
[27] T. L. Daniel, "Cost of locomotion: Unsteady medusan swimming," J. Exp. Biol. **119**, 149 (1985).
[28] P. W. Webb, "Simple physical principles and vertebrate aquatic locomotion," Am. Zool. **28**, 709 (1988).
[29] S. P. Colin and J. H. Costello, "Morphology, swimming performance and propulsive mode of six co-occurring hydromedusae," J. Exp. Biol. **205**, 427 (2002).
[30] M. J. McHenry and J. Jed, "The ontogenetic scaling of hydrodynamics and swimming performance in jellyfish (Aurelia aurita)," J. Exp. Biol. **206**, 4125 (2003).
[31] J. O. Dabiri and M. Gharib, "Sensitivity analysis of kinematic approximations in dynamic medusan swimming models," J. Exp. Biol. **206**, 3675 (2003).
[32] S. Donaldson and G. O. Mackie, "Preliminary observations on escape swimming and giant neurons in Aglantha digitale (Hydromedusae: Trachylina)," Can. J. Zool. **58**, 549 (1980).
[33] S. Childress, personal communication (2008).